Research Square

Preprints are preliminary reports that have not undergone peer review.
They should not be considered conclusive, used to inform clinical practice,
or referenced by the media as validated information.

Fatigue Damage Prediction of Hot Rolling Work Rolls Considering Surface Degradation and Damage Redistribution

Sunrui Tao

sunrui.tao@polimi.it

Yanshan University https://orcid.org/0009-0008-5426-9247

Ruilai Yang

Yanshan University

Jinhang Wang

Yanshan University

Caiyi Liu

Silvia Barella

Yan Peng

Yuhui Wang

Marco Belfi

Wenjing Li

Guoxing Chen

De Li

Carlo Mapelli

Research Article

Keywords: Hot rolling, Work rolls, Fatigue damage prediction, Residual stress

Posted Date: November 18th, 2026

DOI: https://doi.org/10.21203/rs.3.rs-11623066/v1

License: This work is licensed under a Creative Commons Attribution 4.0 International License.
Read Full License

Fatigue Damage Prediction of Hot Rolling Work Rolls Considering Surface Degradation and Damage Redistribution

Sunrui Tao[a,b*], Ruilai Yang[a], Jinhang Wang[a], Caiyi Liu[a,b*], Silvia Barella[b], Yan Peng[a], Yuhui Wang[a], Marco Belfi[b], Wenjing Li[a], Guoxing Chen[d], De Li[a,b,c*], Carlo Mapelli[b]

[a] National Engineering Research Center for Equipment and Technology of Cold Strip Rolling, Yanshan University, Qinhuangdao, 066004, China

[b] Department of Mechanical Engineering, Politecnico di Milano, Milano, 20156, Italy

[c] Department of Electrical Engineering, Qinhuangdao Polytechnic Institute, Qinhuangdao, 066004, China

[d] School of Mechanical and Electronic Engineering, Hubei Polytechnic University, Huangshi, 435003, China

[*] Correspondence: sunrui.tao@polimi.it

Abstract

Hot rolling work rolls are subjected to repeated thermal and mechanical loading, while oxidation and wear alter their surface conditions. This study investigates the effects of residual stress, oxide film evolution, and material removal on fatigue damage in hot rolling work rolls. Residual stresses generated during heat treatment are introduced into a thermomechanical rolling model to determine the local near-surface strain response. Oxide film growth and removal are described using a dynamic model, with predicted thicknesses compared against high-temperature sliding wear measurements. Fatigue damage is evaluated using the Manson-Coffin strain-life relationship and Miner's linear damage rule. Measured roll surface recession and calculated oxide film thickness are used to update the metal-oxide interface position and track fatigue damage redistribution in the remaining material through successive rolling cycles. Initial residual stress increases the peak equivalent strain from 0.0049 to 0.0077 and changes the near-surface fatigue damage distribution. The calculated oxide thickness follows the overall experimental trend, although deviations occur at intermediate wear times. Material removal reduces retained fatigue damage, while changes in oxide film thickness affect its distribution through movement of the metal-oxide interface. Sensitivity analysis shows that wear depth has the greatest influence on retained fatigue damage, with coefficients ranging from -0.82 to -0.85, followed by residual stress and oxidation. These findings support fatigue damage assessment of worn work rolls and may assist in determining suitable regrinding depths.

Keywords: Hot rolling; Work rolls; Fatigue damage prediction; Residual stress

1 Introduction

Work rolls directly participate in the plastic deformation of hot strips and are critical components of hot rolling mills. Their surface condition affects strip profile, dimensional accuracy, surface quality, and rolling stability. During service, the roll surface is repeatedly

subjected to contact with the hot strip, high rolling force, frictional shear, and cyclic water cooling. These conditions generate steep thermal gradients and cyclic mechanical loads in the near surface region. With increasing rolling cycles, wear, oxidation, fatigue cracking, and local spalling gradually develop [1,2]. These degradation mechanisms interact during service. Oxide formation changes the surface contact and wear conditions, while wear continuously removes material in which fatigue damage has accumulated [3,4]. Their interaction governs the evolution of the roll surface and ultimately affects roll life, maintenance frequency, production efficiency, and product quality. A reliable description of these coupled processes is therefore important for predicting work roll life.

The thermal and mechanical behavior of work rolls has been widely investigated. Salehebrahimnejad et al. [5] reported that initial residual stress can significantly alter the stress state of a work roll under subsequent rolling loads. Meng et al. [6] developed a model for predicting roll wear and thermal expansion and applied it to crown and thickness control. Li et al. [7] investigated the temperature field and thermal crown of work rolls. Wang et al. [8] analyzed their thermal behavior during hot rolling. Sabar et al. [9] evaluated rolling force using a combined finite element and neural network approach. These studies have improved the understanding of temperature evolution, contact loading, and roll deformation during hot rolling. However, the initial stress state of the work roll has received relatively limited attention in rolling simulations. This issue is particularly relevant to composite high speed steel (HSS) work rolls. Their working layer and core differ in thermophysical and mechanical properties. During heat treatment, nonuniform thermal deformation and material response can generate a residual stress field within the roll. This residual stress remains before service and forms part of the initial mechanical state for subsequent rolling [5]. During rolling, the initial residual stress interacts with thermal and contact loads and changes the local mechanical response [5,8]. Neglecting this initial state may therefore lead to an incomplete description of the near surface stress and strain response. For fatigue analysis, it is necessary to account for the initial residual stress when determining the strain history of the work roll.

High temperature oxidation is another important aspect of work roll degradation. Wei et al. [10] developed an online method for monitoring the oxidation states of HSS work rolls during hot rolling. Cheng et al. [11] investigated the high-temperature oxidation, friction, and wear behavior of a high-speed steel roll material. Previous studies have shown that oxide formation

and evolution depend on temperature, material composition, exposure conditions, and the surrounding environment [11-13]. Under high temperature tribological conditions, contact and sliding further affect oxide formation and surface degradation [14,15]. The effect of the oxide layer depends on its thickness, continuity, and stability. A compact oxide layer can reduce direct contact between the substrate and the counter surface. In contrast, fracture and detachment of the oxide layer can change the contact and wear conditions [14-16]. During hot rolling, oxide formation and mechanical removal occur continuously [10]. The oxide thickness therefore changes with service time and depends on the competition between oxide growth and removal. Recent numerical studies have also considered surface scale evolution when describing material removal under high temperature conditions [17,18]. A constant oxide thickness cannot adequately represent this dynamic process. A dynamic evolution model is therefore needed to determine the oxide thickness and its effect on substrate material removal.

Work roll life prediction has gradually developed from individual wear or fatigue analysis toward coupled descriptions of surface degradation. Wang et al. [4] proposed a fatigue damage model coupled with wear and showed that material removal affects the accumulated fatigue damage of hot rolling work rolls. Numerical and data driven methods have also been developed to predict roll wear and degradation [19-22]. Opapaiboon et al. [23] investigated the fracture behavior of cast roll materials used in hot rolling. He et al. [24] developed a roll wear model based on surface micro protrusions. Tao et al. [25] combined hot rolling wear experiments with fractal modeling to describe roll wear behavior. These studies provide useful methods for evaluating roll degradation. However, the continuous change in material position caused by progressive surface removal has received less attention in fatigue damage calculations. As wear proceeds, the original surface material is removed and subsurface material gradually becomes exposed. The retained fatigue damage therefore depends not only on damage accumulation but also on the exposure and removal of damaged material.

In this study, a fatigue damage assessment method for hot rolling work rolls is developed by incorporating the initial residual stress state, dynamic oxide evolution, and wear induced material migration. First, the residual stress field is obtained from heat treatment simulation and introduced into a thermomechanical rolling model. The resulting strain history is used for fatigue damage evaluation. Second, a dynamic oxide evolution model is established using the local temperature, contact stress, and sliding conditions. The predicted oxide thickness is

validated by high temperature sliding wear experiments. Finally, the Manson Coffin strain life relation and Miner's linear damage rule are combined with the oxide corrected substrate removal depth. Fatigue damage is accumulated in the material coordinate system to describe the exposure, removal, and redistribution of damaged material during wear. The proposed framework is used to evaluate the evolution and retention of near surface fatigue damage and to clarify the roles of residual stress, oxidation, and progressive material removal in work roll degradation. The resulting fatigue damage distribution with respect to the evolving roll surface provides a basis for assessing near-surface fatigue damage and determining the required grinding depth during off-line roll regrinding.

2 Residual Stress and Rolling Response

2.1 Heat Treatment Residual Stress

The work roll consists of an HSS working layer and a ductile cast iron (DCI)core. The temperature dependent thermal and mechanical properties of the two materials are shown in Fig. 1. Differences in thermal properties, thermal expansion coefficients, and mechanical properties lead to different thermal deformation during heat treatment. The resulting deformation mismatch generates residual stress near the interface and within the roll [26]. The residual stress field after heat treatment is introduced into the subsequent hot rolling simulation as the initial stress state.

The heat treatment process consists of quenching, the first tempering, and the second tempering, as shown in Fig. 2. Before quenching, the roll is heated above 1000 °C and held until a nearly uniform austenitizing temperature is reached [27]. Rapid cooling then produces a large temperature gradient and generates residual stress. Two tempering treatments are subsequently performed. Each tempering treatment includes heating, holding, and cooling. These treatments reduce the residual stress generated during quenching and improve microstructural stability. The residual stress field after the second tempering is used as the initial stress field for the subsequent hot rolling simulation.

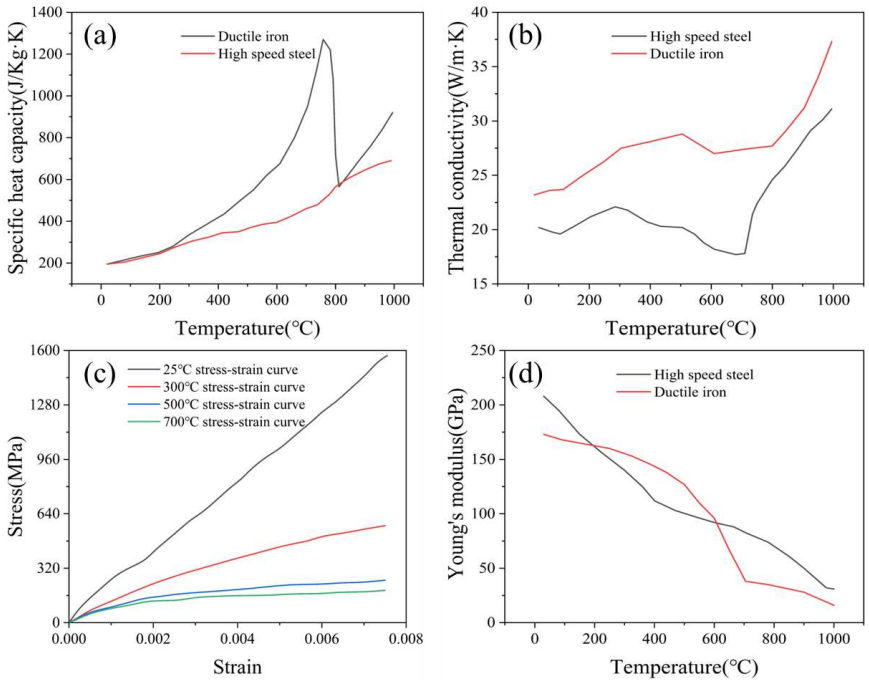


Fig. 1. High temperature properties of rolling mill materials [26]: (a) specific heat capacity, (b) thermal conductivity, (c) Stress-strain for shell, (d) Young's modulus

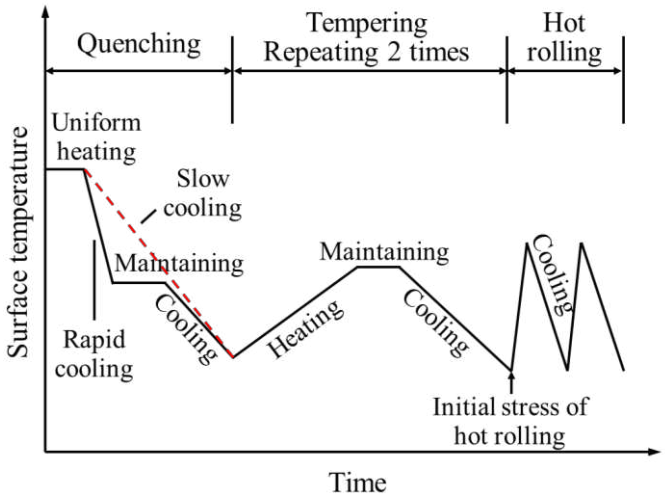


Fig. 2. Surface temperature during heat treatment and hot rolling

Quenching and two tempering treatments were simulated sequentially in Abaqus. After high temperature austenitizing, the roll was assumed to have a uniform initial temperature and a stress free state before quenching [28]. A sequential thermal and mechanical analysis was adopted. The transient temperature field was first calculated and then transferred to the mechanical analysis [26]. Temperature dependent material properties, thermal mismatch between the working layer and core, and thermal elastic plastic behavior were considered.

The model was developed to obtain the initial residual stress field for the subsequent rolling analysis. Phase transformation, transformation plasticity, and creep relaxation were not explicitly modeled, and their effects were represented by equivalent temperature dependent

material properties [28]. The transient temperature field and surface convective boundary condition are described by Eq. 2.1 and 2.2, respectively. These formulations have been widely used in simulations of heat treatment and residual stress evolution in HSS work rolls [29,30].

$$(\rho c_p(T)\frac{\partial T}{\partial t} = \nabla \cdot k(T)\nabla T \tag{2.1}$$

$$-k(T)\frac{\partial T}{\partial n} = h\left(T - T_\infty\right) \tag{2.2}$$

where ρ is the density, c_p is the specific heat capacity, k is the thermal conductivity, T is the temperature, t is the time, h is the convective heat transfer coefficient, T_∞ is the ambient temperature, and n is the outward normal direction. The corresponding thermal boundary conditions were applied during quenching and the two tempering stages [31].

The total strain in the roll is expressed by Eq. 2.3:

$$\varepsilon = \varepsilon^e + \varepsilon^p + \varepsilon^{\text{th}} \tag{2.3}$$

The thermal strain increment is given by Eq. 2.4:

$$\Delta\varepsilon^{\text{th}} = \alpha(T)\Delta T I \tag{2.4}$$

where $\varepsilon^{\text{e}}, \varepsilon^{\text{p}}, \varepsilon^{\text{th}}$ are the elastic, plastic, and thermal strains, respectively. $\alpha(T)$ is the temperature dependent coefficient of thermal expansion, and I is the second order identity tensor. The thermal conductivity, specific heat capacity, coefficient of thermal expansion, elastic modulus, and yield strength were all considered temperature dependent.

2.2 Thermomechanical Rolling Response

The numerical analysis comprised heat transfer calibration, residual stress calculation and transfer, thermomechanical rolling analysis, strain history extraction, and fatigue damage calculation. A cyclic heat transfer model was established for the work roll. The residence time of a surface material point in the rolling, water cooling, and air cooling regions was determined from the roll speed and the central angle of each region, and the corresponding thermal boundary conditions were applied. The initial strip temperature was 1000 °C, while the cooling water and ambient temperatures were 30 °C. Thermal contact was defined between the strip and the work roll, while heat flux in the other regions was applied through the DFLUX subroutine. The initial heat transfer coefficients were obtained from previous studies and calibrated against the measured work roll temperature after rolling [4,7]. The calibrated parameters were then used in the thermomechanical rolling analysis to reproduce the work roll temperature field under operating conditions [25]. A two dimensional plane strain thermomechanical model of a four high mill was developed using a representative cross section

subjected to a high rolling load, as shown in Fig. 3. The main parameters are listed in Table 1. Uniform deformation and loading were assumed along the roll axis. Axial variations and roll edge effects were neglected. The analysis focused on the near surface thermomechanical response of the work roll. The work roll and strip were meshed with four node coupled temperature displacement elements (CPE4RT). The mesh was gradually refined toward the work roll surface, with further refinement in the strip contact region. A coarser mesh was used for the backup roll.

Table 1. Parameters of the work roll during hot rolling

Parameters	Value
Velocity of the work roll / $m \cdot s^{-1}$	1.41
Rolling force [kN]	16800
Work roll diameter / mm	750
Rolling reduction / mm	3
Initial work roll temperature / °C	30
Entry strip temperature / °C	1000
Air/water temperature / °C	30
Entry strip width / mm	1200
Water pressure / MPa	1.5
Water flow / $L \cdot min^{-1}$	2500
Heat transfer coefficient	Deformation region 45,000 W $(m^2 \cdot K)^{-1}$ Wiper cooling 14,600 W $(m^2 \cdot K)^{-1}$ Water cooling 32,600 W $(m^2 \cdot K)^{-1}$ Air cooling 5 W $(m^2 \cdot K)^{-1}$

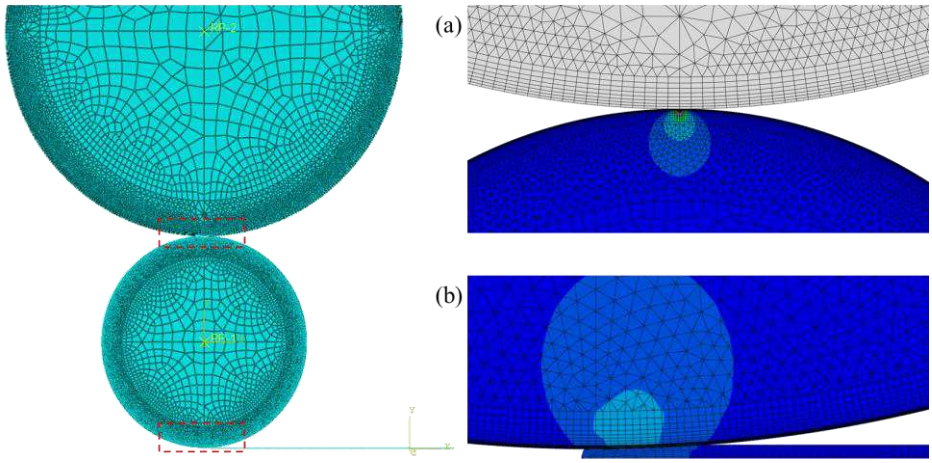


Fig. 3. Finite element model: (a) work roll and backup roll contact region, (b) rolling deformation region

The radial, circumferential, and axial residual stresses obtained from the heat treatment model were fitted as continuous functions of depth. Because the heat treatment and rolling models had different meshes, the fitted stress profiles were assigned to the integration points through the

SIGINI subroutine. The resulting stress field was used as the initial condition for the thermomechanical rolling analysis.

The depth from the roll surface for an integration point is given by Eq. 2.5.

$$d = R - \sqrt{x^2 + y^2} \tag{2.5}$$

where R is the work roll radius, and x^2 and y^2 are the coordinates of the integration point relative to the roll center. d is the radial depth measured from the current roll surface. The SIGINI subroutine determines the radial, circumferential, and axial residual stresses according to d. These stress components are then transformed from the cylindrical coordinate system into the complete stress tensor of the rolling model. The axial residual stress is transferred as the out of plane stress component in the two-dimensional plane strain model.

Two rolling models with and without initial residual stress were established. The residual stress field was introduced through the SIGINI subroutine, while zero initial stress was assigned to the reference model. All other model settings were identical. Stress and strain histories at the critical location were extracted for subsequent fatigue damage calculation. The detailed simulation procedure is summarized in Table 2.

Table 2. Boundary conditions of the finite element model

Step	Load	Boundary
a. Initial residual stress	Predefined Field: Stress	None
b. Contact	None	roll vertical displacement
c. Reduction	None	roll vertical displacement
d. Rolling	Heat flux on work roll surface	Work roll rotation

2.3 Finite Element Results

2.3.1 Residual Stress Distribution

Fig. 4 shows the radial distribution of residual stress on the roll end face after quenching and tempering. After quenching, the stress gradually changed from about 330 MPa in tension near the roll center to about -540 MPa in compression near the outer edge. Tempering caused a clear relaxation of the residual stress. The tensile stress near the center decreased to about 200 MPa, while the compressive stress near the outer edge decreased to about -460 MPa. The stress magnitude and radial gradient were also reduced, resulting in a smoother distribution. These results indicate that tempering released part of the residual stress generated during quenching while retaining compressive stress near the roll surface. Given the simplifying assumptions of the model, the results are not regarded as a strict quantitative validation. Nevertheless, the predicted stress levels and radial variation fall within the ranges reported for hot rolling work

rolls and large forged steel rolls [26,27,31]. The calculated residual stress field was therefore used as the initial state for the subsequent thermomechanical rolling analysis.

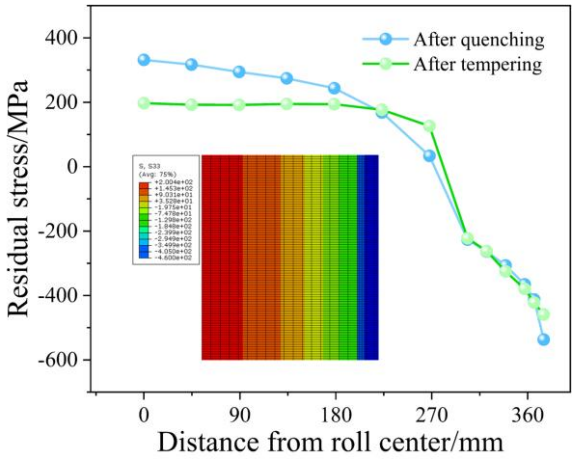


Fig. 4. Radial distribution of residual stress on the roll surface after quenching and tempering

2.3.2 Rolling Strain Response

Fig. 5 shows the maximum principal strain and equivalent plastic strain at the monitored point on the work roll surface. Results are compared for the cases with and without initial residual stress. Once contact was established, the maximum principal strain rapidly reached its peak and then gradually decreased. The equivalent plastic strain accumulated mainly during the initial contact stage and remained nearly constant thereafter.

Without initial residual stress, the peak maximum principal strain was approximately 0.0048. It increased to about 0.0071 when initial residual stress was included, corresponding to an increase of approximately 48%. After reaching the peak, the maximum principal strain gradually stabilized in both cases. A short fluctuation occurred between 0.80 and 0.90 s due to changes in the contact load between the work roll and backup roll. The maximum principal strain remained higher throughout the simulation when initial residual stress was included. This result indicates that initial residual stress increased the local strain level at the monitored point. The final equivalent plastic strain was approximately 0.0028 without initial residual stress and 0.0032 with initial residual stress. This corresponds to an increase of about 14%. In both cases, plastic strain developed mainly during the initial contact stage, with no clear further accumulation thereafter. Under the simulated conditions, initial residual stress therefore increased the peak maximum principal strain and moderately promoted local plastic deformation [26].

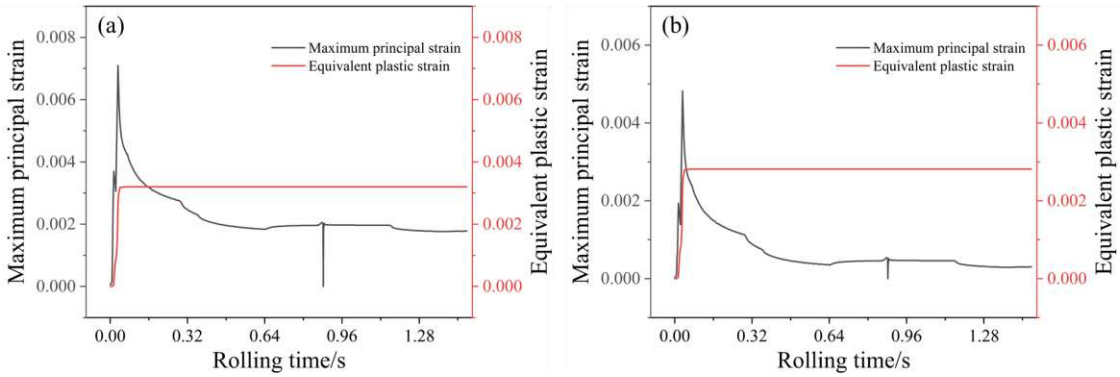


Fig. 5. Effect of initial residual stress on the strain response at the work roll surface: (a) with initial residual stress, (b) without initial residual stress

To characterize the local multiaxial strain state, the von Mises equivalent strain was calculated from the three total principal strains at the same material point and time using Eq. 2.6 [26].

$$\Delta\varepsilon_{eq} = \frac{\sqrt{2}}{3}\sqrt{(\Delta\varepsilon_1 - \Delta\varepsilon_2)^2 + (\Delta\varepsilon_2 - \Delta\varepsilon_3)^2 + (\Delta\varepsilon_3 - \Delta\varepsilon_1)^2} \tag{2.6}$$

Where $\Delta\varepsilon_1, \Delta\varepsilon_2, \Delta\varepsilon_3$ are the maximum, intermediate, and minimum principal strains at the same material point and time. The von Mises equivalent strain is used to characterize the local distortion of the strain state. The results are shown in Fig. 6. In both cases, the equivalent strain increased rapidly to a peak during the initial loading stage and then gradually decreased to a stable level. Without the initial residual stress, the peak equivalent strain was about 0.0049. With the initial residual stress, it increased to about 0.0077, corresponding to an increase of approximately 57%. The equivalent strain also remained higher throughout the subsequent rolling process, indicating that the initial residual stress increased the local distortion strain and intensified strain concentration during cyclic contact [26].

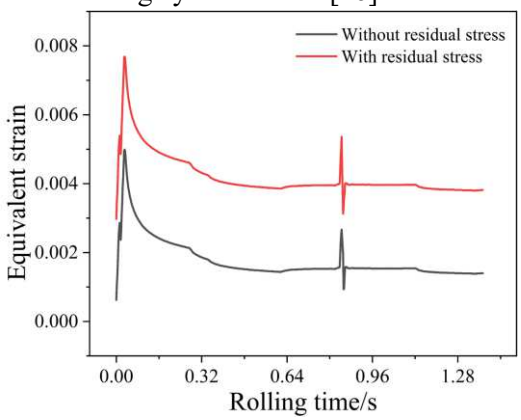


Fig. 6. Effect of initial residual stress on the equivalent strain response at the work roll surface

Although the work roll and backup roll contact region was subjected to high contact stress, the equivalent plastic strain remained close to 0, indicating that no significant plastic deformation occurred under the present loading and material conditions [4,5]. In contrast, the monitored point in the rolling region exhibited higher equivalent plastic strain and von Mises equivalent

strain, indicating more severe local deformation and a higher risk of fatigue damage. Therefore, the fatigue analysis focused on the critical location in the rolling region.

3 Modeling and Validation of Oxidation Evolution

3.1 Hot Rolling Wear Tests

To characterize oxide film formation on the work roll surface under hot rolling conditions, a high temperature sliding wear test rig was developed for HSS roll material, as shown in Fig. 7. The test rig was designed to reproduce the combined effects of high temperature and friction during rolling. The main experimental parameters are listed in Table 3.

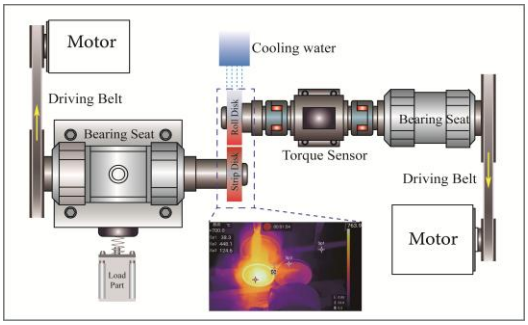


Fig. 7. Schematic of the high temperature sliding wear test device [25]

Table 3. Experimental parameters of the high-temperature twin-disc wear tests

Parameter	Value	Parameter	Value
Test temperature	450℃	Work roll size	φ70mm
Load	1000N	Strip size	φ60mm
Initial roughness	Ra＜0.5μm	Work roll speed	780rpm
Test time	10/20/40/80min	Strip speed	850rpm

As shown in Fig. 8, SEM observations reveal that a continuous oxide film forms on the worn surface after high temperature sliding. The oxide film evolves with sliding time, accompanied by local cracking, fragmentation, and spallation. These features indicate the continuous formation and removal of the oxide film during sliding. Therefore, the oxide film thickness is governed by the competition between oxide growth and wear removal. Based on this mechanism, a dynamic oxide film evolution model was established by considering both processes [25,32,33].

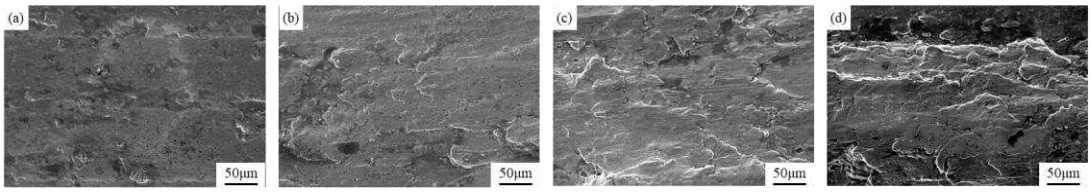


Fig. 8. SEM images of the worn surface after high temperature sliding: (a) 10min, (b) 20min, (c) 40min, (d) 80min.

3.2 Oxidation Evolution Model

3.2.1 Model Assumptions

During hot rolling, the work roll surface experiences strip heating, rolling loading, sliding friction, and cooling in each revolution. The oxide film thickness is governed by the competition between high temperature oxidation and wear removal rather than by static oxidation alone [34]. The oxide film thickness, h_{ox} is treated as a time dependent state variable. The following assumptions are adopted:

(a) Oxide growth is dominated by diffusion at elevated temperature.

(b) The oxygen concentration profile within the oxide layer is assumed to be quasi steady during each time increment.

(c) Rolling load and frictional shear influence the growth kinetics and stability of the oxide layer.

(d) The oxide layer is continuously removed by sliding wear in the rolling deformation zone.

The evolution of oxide film thickness is expressed as Eq. 3.1 [35]:

$$\frac{dh_{ox}}{dt} = \left(\frac{dh_{ox}}{dt}\right)_{growth} - \left(\frac{dh_{ox}}{dt}\right)_{removal} \tag{3.1}$$

The first term represents oxide growth, whereas the second term represents oxide removal by wear during rolling contact.

3.2.2 Oxidation Growth Model

Oxide growth at elevated temperature is controlled by ionic diffusion through the existing oxide layer. As the oxide layer becomes thicker, the diffusion path increases and the growth rate decreases. Under the steady diffusion assumption, the oxide growth rate is expressed as Eq. 3.2:

$$\left(\frac{dh_{ox}}{dt}\right)_{growth} = \frac{k_g}{h_{ox}} \tag{3.2}$$

Where k_g is the oxide growth coefficient. The oxide growth coefficient is temperature dependent and can be expressed using the Arrhenius equation [36]:

$$k_g(T) = k_0 \exp\left(-\frac{Q}{RT}\right) \tag{3.3}$$

where k_0 is the pre exponential factor, Q is the apparent activation energy for oxide growth, R is the universal gas constant, and T is the temperature of the roll surface.

During hot rolling, the work roll surface is subjected to both normal pressure and frictional shear stress. The stress state changes the effective activation energy of oxidation. As a result, the oxide growth rate is modified [34,35]. To account for this effect, a stress assisted oxidation

term is introduced to describe the influence of mechanical loading on oxide growth, as given in Eq. 3.4.

$$k_g(T,\sigma_{\mathrm{eq}}) = k_0 \exp\left(-\frac{Q}{RT}\right)\exp\left(\frac{\gamma\sigma_{\mathrm{eq}}}{RT}\right) \tag{3.4}$$

where γ is the stress coefficient, and σ_{eq} is the equivalent contact stress.

For the strip and work roll contact interface, the equivalent contact stress is given by:

$$\sigma_{\mathrm{eq}} = \sqrt{p^2 + 3\tau^2} \tag{3.5}$$

$$\tau = \mu p \tag{3.6}$$

where p is the local rolling pressure, τ is the frictional shear stress, and μ is the coefficient of friction, which is determined by rolling theory [37].

Substituting Eq. 3.4-3.6 into Eq. 3.2 gives the oxide growth rate on the work roll surface during hot rolling:

$$\left(\frac{dh_{\mathrm{ox}}}{dt}\right)_{\mathrm{growth}} = \frac{k_0 \exp\left(-\frac{Q}{RT}\right)\exp\left(\frac{\gamma\sqrt{p^2+3(\mu p)^2}}{RT}\right)}{h_{\mathrm{ox}}} \tag{3.7}$$

Eq. 3.7 indicates that oxide growth is primarily controlled by temperature. The equivalent contact stress is introduced as a mechanical correction to account for the influence of rolling pressure and frictional shear on the oxidation kinetics.

In the rolling deformation zone, the oxide layer grows continuously and is removed by sliding between the strip and the work roll. The oxide thickness is therefore governed by the competition between growth and removal. Based on the Archard wear law [35,37], the oxide removal rate is expressed as Eq. 3.8:

The removal term in Eq. 3.8 represents the mechanical loss of the oxide layer during sliding contact and is used only to determine the retained oxide film thickness. It does not represent the removal depth of the metallic substrate used in the subsequent fatigue damage migration calculation.

$$\left(\frac{dh_{\mathrm{ox}}}{dt}\right)_{\mathrm{removal}} = \frac{K_{\mathrm{eff}}(h_{\mathrm{ox}})pv_s}{H} \tag{3.8}$$

where K_{eff} is the effective wear coefficient, v_s is the local sliding velocity, and H is the effective surface hardness used in the wear calculation.

$$K_{\mathrm{eff}}(h_{\mathrm{ox}}) = K_{\mathrm{ox}} + (K_{\mathrm{mech}} - K_{\mathrm{ox}})\exp\left(-\frac{h_{\mathrm{ox}}}{h_c}\right) \tag{3.9}$$

where K_{mech} is the mechanical wear coefficient of the exposed metal substrate, K_{ox} is the

wear coefficient when the surface is sufficiently covered by the oxide layer, and h_c is the characteristic oxide thickness required to protect the substrate. When $h_{\mathrm{ox}} = 0$, $K_{\mathrm{mech}} = K_{eff}$. The substrate is then directly involved in contact, resulting in severe wear. As the oxide thickness increases, K_{eff} gradually decreases.

When $h_{ox} \square h_c$, K_{eff} approaches K_{ox}, indicating that the wear state becomes stable after sufficient oxide coverage [25,35].

By combining oxide growth with wear removal, the evolution equation for the oxide thickness on the hot rolling work roll surface is obtained as Eq. 3.10:

$$\frac{dh_{\mathrm{ox}}}{dt} = \frac{k_0 \exp\left(-\frac{Q}{RT}\right)\exp\left(\frac{\gamma\sigma_{\mathrm{eq}}}{RT}\right)}{h_{\mathrm{ox}}} - \frac{K_{\mathrm{eff}}(h_{\mathrm{ox}})pv_s}{H} \tag{3.10}$$

Eq. 3.10 shows that the oxide thickness on the work roll surface is governed by the competition between oxide growth and wear removal. The first term represents the oxide growth rate. It is mainly controlled by temperature and is also affected by contact stress. The second term represents the wear removal rate. It depends on rolling pressure, local sliding velocity, material hardness, and oxide coverage [14,25].

An explicit time stepping scheme was used to determine the evolution of oxide thickness. At the i_{th} time step, the oxide thickness is updated as:

$$h_{\mathrm{ox}}^{i+1} = h_{\mathrm{ox}}^{i} + \left[\frac{k_g(T_i,\sigma_{\mathrm{eq},i})}{h_{\mathrm{ox}}^{i}} - \frac{K_{\mathrm{eff}}(h_{\mathrm{ox}}^{i})p_i v_{s,i}}{H}\right]\Delta t \tag{3.11}$$

To avoid the numerical singularity in the oxide growth term at $h_{\mathrm{ox}} = 0$, a small initial oxide thickness is introduced as $h_{\mathrm{ox}}(0) = h_{ox,0}$, where $h_{ox,0}$ may represent the thickness of the native oxide layer or a small positive initial value. To ensure physical consistency, the oxide thickness is constrained to remain nonnegative as $h_{\mathrm{ox}}^{i+1} = \max(h_{\mathrm{ox}}^{i+1}, 0)$. The temporal evolution of the oxide thickness on the work roll surface during hot rolling is obtained through the above time stepping procedure.

3.3 Model Validation

To validate the proposed oxide film evolution model, the wear tests were interrupted after 10, 20, 40, and 80 min. Cross sections were prepared from specimens at each wear stage and examined by SEM. Representative cross sectional features of the oxide film at different stages are shown in Fig. 9. To reduce the influence of local thickness variations, the oxide film thickness was measured at multiple locations on several cross sections for each specimen. The values were used for model validation. The SEM observations show that a relatively continuous

oxide layer formed on the worn surface, with a clear interface between the oxide layer and the substrate. The film thickness varied locally along the cross section, indicating spatial differences in oxide growth and wear removal during high temperature sliding. This nonuniformity may result from local variations in oxidation and material removal under contact stress and frictional shear [1,25,32]. Fig. 10 compares the predicted and experimentally measured oxide film thicknesses as a function of test time. The predicted oxide film thickness increases rapidly during the initial stage, followed by a gradual reduction in the growth rate. Although the growth rate decreases with increasing time, the predicted thickness continues to increase, reaching approximately 20 μm at 80 min. The experimental measurements show a similar overall increasing trend, with the oxide film thickness rising from approximately 4-7 μm at 10 min to 17-22 μm at 80 min. However, noticeable deviations are observed between the predicted and measured values, particularly during the intermediate stage (20-40 min), where the model tends to overestimate the oxide film thickness. At longer test times, the predicted values fall within the range of experimental measurements. The decreasing growth rate is consistent with the combined effects of progressive oxidation and continuous oxide removal by sliding wear, which limit the net accumulation of the oxide film. The model captures the general evolution of oxide film thickness under high-temperature sliding conditions, exhibiting a trend similar to that reported in Ref. [11], although some quantitative discrepancies remain.

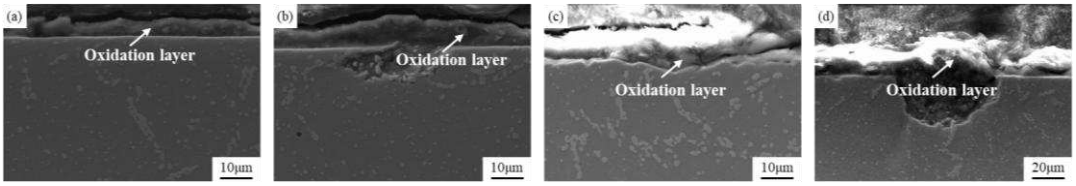


Fig. 9. Representative cross sectional morphologies of the oxide film at different wear times: (a) 10 min, (b) 20 min, (c) 40 min, (d) 80 min

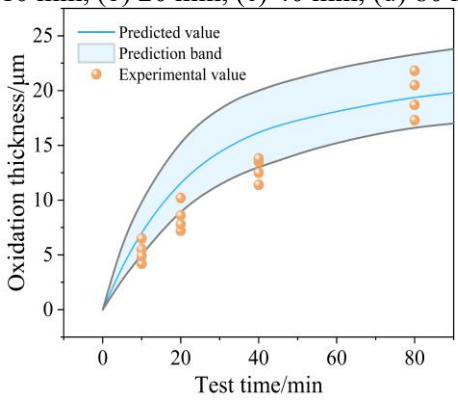


Fig. 10. Comparison of predicted and measured oxide film thicknesses

4 Coupled Fatigue Life Prediction

4.1 Fatigue Life Model

During hot rolling, the work roll surface repeatedly enters and leaves the rolling zone as the roll rotates. The surface is subjected to cyclic thermal and mechanical loading. When the local strain exceeds the elastic range, cyclic plastic deformation occurs and may lead to low cycle fatigue [28,29]. Therefore, the equivalent strain range in the rolling zone was selected as the fatigue parameter. The strain life relationship was then used to estimate the fatigue life of the work roll surface.

Under multiaxial loading, the von Mises equivalent strain range was calculated from the ranges of the three principal strains during one loading cycle using Eq. 2.6 [4]. The corresponding equivalent strain amplitude was then used as the fatigue parameter in the strain life relation:

$$\varepsilon_{a,eq} = \frac{\Delta\varepsilon_{eq}}{2} \tag{4.1}$$

$$\varepsilon_{a,eq} = \frac{\sqrt{2}}{6}\sqrt{(\Delta\varepsilon_1 - \Delta\varepsilon_2)^2 + (\Delta\varepsilon_2 - \Delta\varepsilon_3)^2 + (\Delta\varepsilon_3 - \Delta\varepsilon_1)^2} \tag{4.2}$$

Where $\Delta\varepsilon_1, \Delta\varepsilon_2, \Delta\varepsilon_3$ are the ranges of the maximum, intermediate, and minimum principal strains during one loading cycle, respectively. The equivalent strain amplitude is then introduced into the strain life relation Eq. 4.3:

$$\varepsilon_{a,eq} = \frac{\sigma_f^{'}}{E}(2N_f)^b + \varepsilon_f^{'}(2N_f)^c \tag{4.3}$$

where N_f is the number of cycles to fatigue failure, E is Young's modulus, $\sigma_f^{'}$ and $\varepsilon_f^{'}$ are the fatigue strength coefficient and fatigue ductility coefficient, respectively, and b and c are the fatigue strength exponent and fatigue ductility exponent, respectively.

These parameters are normally obtained from strain-controlled fatigue tests. Considering the time and cost required for such tests, when complete cyclic test data are unavailable, the Manson universal slopes method is used to approximate the relationship between strain range and fatigue life from the material's monotonic tensile properties in Eq. 4.4:

$$\varepsilon_{a,eq} = 1.75\frac{\sigma_{uts}}{E}N_f^{-0.12} + 0.5D^{0.6}N_f^{-0.6} \tag{4.4}$$

where σ_{uts} is the ultimate tensile strength of the material, and D is the true fracture ductility, which can be calculated from the reduction of area ψ [38,39]:

$$D = \ln\left(\frac{1}{1-\psi}\right) = -\ln(1-\psi) \tag{4.5}$$

The equivalent strain amplitude used in Eq. 4.4 was determined from the strain range over a complete loading cycle using Eqs. 4.1 and 4.2. The corresponding fatigue life was then obtained

by numerically solving Eq. 4.4. Because Eq. 4.4 contains terms with different negative powers of N_f, the fatigue life N_f at the corresponding location is generally determined by numerical iteration. When the load level varies from one work-roll revolution to another, the total fatigue damage is calculated using the linear cumulative damage rule. If the fatigue life corresponding to the i_{th} load level is $N_{f,i}$ and the actual number of cycles experienced is n_i, the damage fraction caused by that load level is:

$$d_i = \frac{n_i}{N_{f,i}} \tag{4.6}$$

The damage contributions from all load levels are summed linearly, as given in Eq. 4.7:

$$D_{tot} = \sum_{i=1}^{m} \frac{n_i}{N_{f,i}} \tag{4.7}$$

Fatigue failure is assumed to occur when the cumulative damage reaches 1. Under steady rolling conditions, a surface material point enters the rolling zone once per revolution of the work roll. This may be approximated as one principal strain cycle. If the fatigue life associated with this cycle is $N_{f,i}$, the damage per revolution is:

$$d_{rev} = \frac{1}{N_{f,r}} \tag{4.8}$$

After n_{rev} cumulative revolutions of the work roll, the damage at a surface material point in the rolling zone is:

$$D_r = n_{rev} d_{rev} = \frac{n_{rev}}{N_{f,r}} \tag{4.9}$$

Therefore, when load fluctuations and other damage mechanisms are neglected, the theoretical number of work roll revolutions to fatigue failure is approximately $N_{f,r}$. If the backup roll contact zone remains within the elastic strain range, its low cycle fatigue damage is generally much smaller than that in the rolling zone. Accordingly, this section takes the rolling zone, where pronounced cyclic plastic deformation occurs, as the primary region for fatigue-life assessment.

4.2 Coupled Prediction Method

During hot rolling, fatigue damage accumulates near the work roll surface under cyclic thermal and mechanical loading. Wear and high temperature oxidation occur simultaneously. The cumulative wear depth is determined from measured work roll surface profile changes. For the fatigue damage calculation, the measured wear depth is distributed uniformly over the prescribed rolling cycles. Wear removes surface material and its accumulated fatigue damage, while oxidation changes the position of the metal-oxide interface [6,9,19,37]. Wear removes surface material and the associated fatigue damage, causing the remaining damage distribution

to shift toward the roll surface. The evolution of the oxide film modifies the position of the metal-oxide interface, thereby affecting the redistribution of retained fatigue damage within the remaining metallic substrate. Based on this mechanism, the oxide film thickness is introduced into the wear fatigue model to describe fatigue damage evolution under oxidation and wear. The overall procedure for fatigue life prediction is shown in Fig. 11.

The following assumptions are adopted: (1) fatigue damage accumulation follows Miner's linear damage rule, (2) the measured wear depth is distributed uniformly over the prescribed rolling cycles in the baseline calculation, and (3) the total profile wear is sufficiently small relative to the work roll radius that changes in the local thermomechanical loading field can be neglected. These assumptions allow the previously calculated cyclic strain field to be used for fatigue damage assessment while explicitly accounting for the changing position of the metallic substrate.

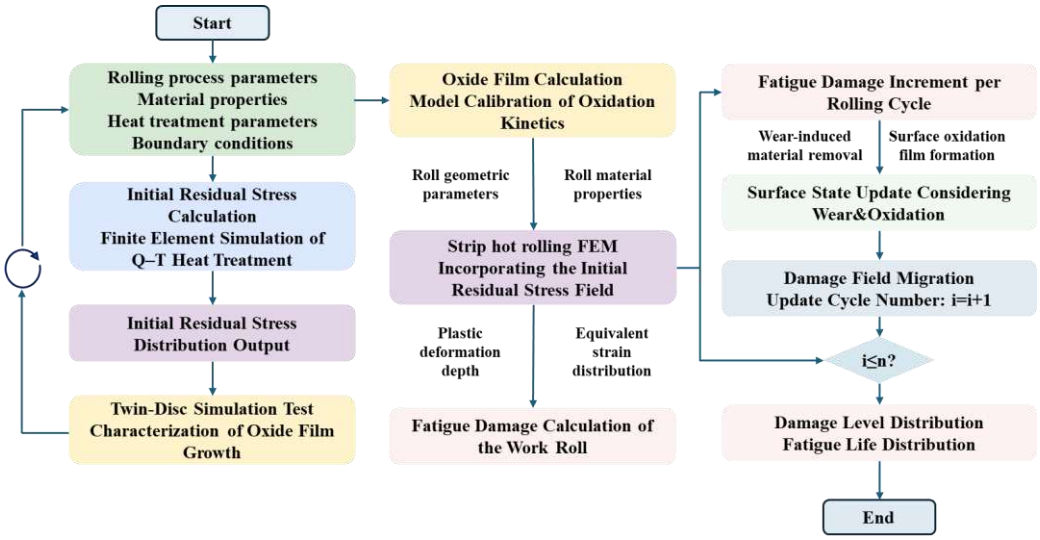


Fig. 11. Flowchart for fatigue life prediction of the hot rolling work roll

I. Geometrical relationship between the external surface and metallic substrate

The instantaneous external radius of the work roll is defined as the sum of the metal-oxide interface radius and the residual oxide film thickness, as shown in Eq. 4.10.

$$R_{out,i} = R_{m,i} + h_{ox,i} \tag{4.10}$$

where $R_{\mathrm{out},i}$ and $R_{\mathrm{m},i}$ denote the external surface radius and the metal-oxide interface radius after rolling cycle i, respectively. $h_{\mathrm{ox},i}$ is the residual oxide film thickness obtained from the oxidation evolution model in Section 3.

The cumulative wear is defined as in Eq. 4.11:

$$W_{\mathrm{app},i} = R_{\mathrm{out},0} - R_{\mathrm{out},i} \tag{4.11}$$

Similarly, the cumulative recession of the metal and oxide interface is defined as in Eq.4.12:

$$W_{\mathrm{int},i} = R_{\mathrm{m},0} - R_{\mathrm{m},i} \tag{4.12}$$

Combining these definitions with Eq. 4.11 gives:

$$W_{\mathrm{int},i} = W_{\mathrm{app},i} + h_{\mathrm{ox},i} - h_{\mathrm{ox},0} \tag{4.13}$$

where $h_{\mathrm{ox},0}$ is the initial oxide film thickness. The metal-oxide interface recession describes the geometrical change of the remaining metallic substrate associated with both mechanical material removal and oxidation-induced interface movement. It should therefore not be interpreted solely as mechanical wear depth. Taking an industrial hot-rolling production line as an example, the work roll wear depth was 0.7 mm after 9000 rolling cycles. Accordingly, an average wear depth per cycle is used as a prescribed input for the damage redistribution calculation, rather than being independently predicted by the present model. The measurement was performed with the residual oxide film retained on the roll surface. The corresponding incremental metal-oxide interface recession is:

$$\Delta W_{\mathrm{int},i} = \Delta W_{\mathrm{app},i} + h_{\mathrm{ox},i} - h_{\mathrm{ox},i-1} \tag{4.14}$$

The residual oxide thickness $h_{\mathrm{ox},i}$ is directly evaluated from the time-dependent evolution model in Section 3 at the corresponding rolling time. No additional oxide wear correction or empirical substrate protection coefficient is introduced.

II. Fatigue damage accumulation and material-coordinate transformation

To track the fatigue damage retained within the metallic substrate, a fixed material coordinate x is defined as the initial depth of a material point below the metal-oxide interface. As the interface recedes, the depth of the same material point relative to the current interface changes, as shown in Eq. 4.15:

$$r_i = x - W_{\mathrm{int},i} \tag{4.15}$$

where r_i is the depth after cycle i. Material points satisfying ($x < W_{\mathrm{int},i}$) no longer belong to the remaining metallic substrate and are excluded from subsequent fatigue damage accumulation. During each rolling cycle, fatigue damage is first accumulated at the material positions defined before the current interface recession. According to Miner's linear damage rule, the cumulative damage before the geometrical update is given by Eq. 4.16:

$$D_i^*(r) = D_{i-1}(r) + d_i(r) \tag{4.16}$$

where $D_{i-1}(r)$ is the cumulative damage after the preceding cycle, and $d_i(r) = 1/N_{f,i}(r)$ is the incremental fatigue damage generated during the current cycle. The fatigue life $N_{f,i}(r)$ is determined from the strain-life relationship described in Section 4.1. Both terms on the right-hand side are evaluated using the depth coordinate associated with the interface at the beginning of cycle i. Following fatigue damage accumulation, the metal-oxide interface is updated

according to Eq. 4.12. The remaining damage distribution is then transformed to the new surface-relative coordinate system:

$$D_i\,(r) = D_i^{*}\,(r + \Delta W_{\mathrm{int},i}) \tag{4.17}$$

This transformation ensures that the cumulative damage remains associated with the same metallic material points while their positions relative to the evolving interface change. Combining Eq. 4.14 and Eq. 4.15, the fatigue damage recurrence relation becomes:

$$D_i\,(r) = D_{i-1}(r + \Delta W_{\mathrm{int},i}) + d_i(r + \Delta W_{\mathrm{int},i}) \tag{4.18}$$

The incremental damage and previously accumulated damage are therefore evaluated consistently at the corresponding material positions before the geometrical update. For multiple rolling cycles, the cumulative damage at a remaining material point can be expressed as in Eq. 4.19:

$$D_i\,(r) = D_0(r + W_{\mathrm{int},i}) + \sum_{k=1}^{i} d_k\,(r + W_{\mathrm{int},i} - W_{\mathrm{int},k-1}) \tag{4.19}$$

where D_0 denotes the initial damage distribution and k is the rolling cycle index. If the work roll is initially assumed to be free of fatigue damage, $D_0 = 0$.

III. Final interface position and limiting condition

Since the roll surface profile was measured before the residual oxide film was removed, the retreat of the metal-oxide interface after N rolling passes can be calculated using Eq. 4.20:

$$W_{\mathrm{int},N} = W_{app,N} + h_{ox,N} - h_{ox,0} \tag{4.20}$$

Thus, the final metal-oxide interface recession is calculated from the measured roll surface profile change after service and the change in residual oxide film thickness. In the limiting case without an oxide film, $h_{\mathrm{ox},i} = h_{\mathrm{ox},i-1} = 0$, and Eq. 4.18 reduces to:

$$D_i(r) = D_{i-1}\left(r + \Delta W_{\mathrm{app},i}\right) + d_i\left(r + \Delta W_{\mathrm{app},i}\right) \tag{4.21}$$

This limiting expression describes fatigue damage accumulation and redistribution caused by metallic surface recession without oxidation. The coupled calculation procedure is shown in Fig. 12. The cyclic strain amplitude and fatigue life are calculated using the thermomechanical rolling simulation and the fatigue model in Section 4.1. The residual oxide film thickness is obtained from the oxidation model in Section 3. The metal-oxide interface recession is then calculated from the measured surface profile change and the residual oxide film thickness. Fatigue damage is accumulated at the corresponding material positions, and the retained damage field is updated to account for surface wear. These calculations are repeated for each rolling cycle until the specified number of cycles is reached.

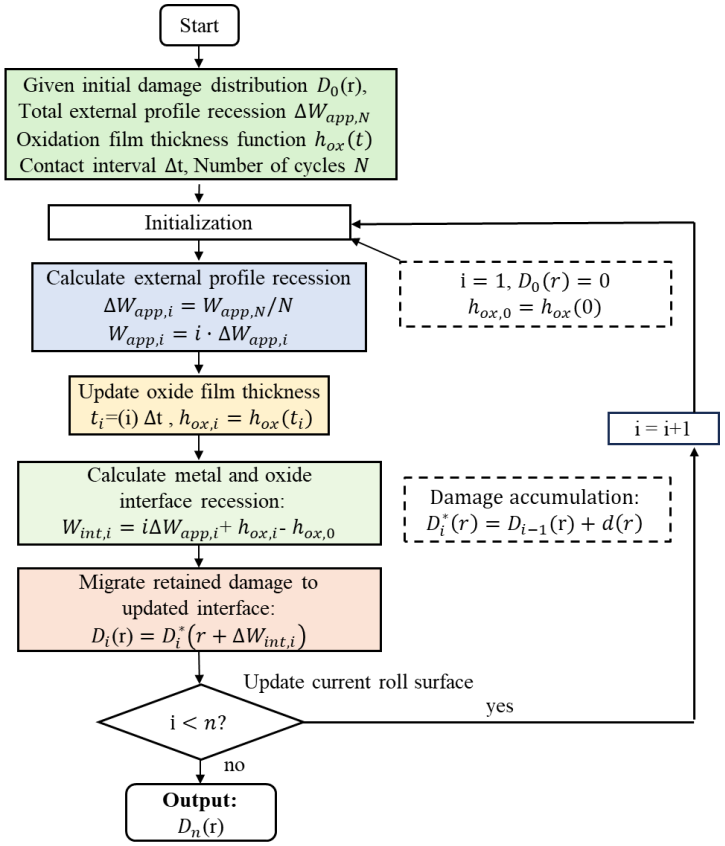


Fig. 12. Computational procedure for fatigue damage redistribution considering wear and oxidation

4.3 Fatigue Damage Analysis

Fig. 13(a) shows a comparison of the depth-mapped fatigue life distributions under four conditions. As expected, the predicted fatigue life increases with depth in all cases, reflecting the decrease in cyclic strain towards the roll interior. Without surface degradation, the predicted fatigue life is lowest. When wear is included, higher fatigue-life values are observed in the remaining metallic substrate. A further increase is observed when oxidation is considered. These differences primarily reflect the redistribution of the reference fatigue-life field following surface recession rather than an improvement in the intrinsic fatigue resistance or the actual remaining service life of the roll material. The effect of initial residual stress varies with radial depth. As can be seen in the enlarged view, the predicted fatigue life is slightly lower near the surface when initial residual stress is included. However, beyond approximately 0.07 mm, it becomes higher than that obtained with wear and oxidation alone. This variation is associated with the depth-dependent influence of initial residual stress on local cyclic strain [28,29]. Fig. 13(b) shows the radial distribution of retained fatigue damage under the same conditions. Fatigue damage decreases with depth in all cases and is concentrated near the roll surface. The highest damage is obtained without surface degradation. When wear is considered, the retained

damage decreases markedly because part of the previously damaged surface layer is removed. Including oxidation leads to a further slight reduction in retained damage. This difference is associated with changes in metal-oxide interface recession and the redistribution of accumulated damage in the remaining substrate [25,32]. Initial residual stress has a greater effect near the surface. The predicted surface damage increases from approximately 0.23 to 0.37 when initial residual stress is included. However, this difference decreases with depth. Beyond approximately 0.08 mm, the retained damage becomes slightly lower than that obtained without initial residual stress. This trend is consistent with the fatigue life distribution in Fig. 13(a). Overall, wear mainly affects retained damage through the removal of previously damaged material, while oxidation changes the position of the metal-oxide interface and the resulting damage distribution. Initial residual stress influences the local fatigue response by changing the cyclic strain distribution.

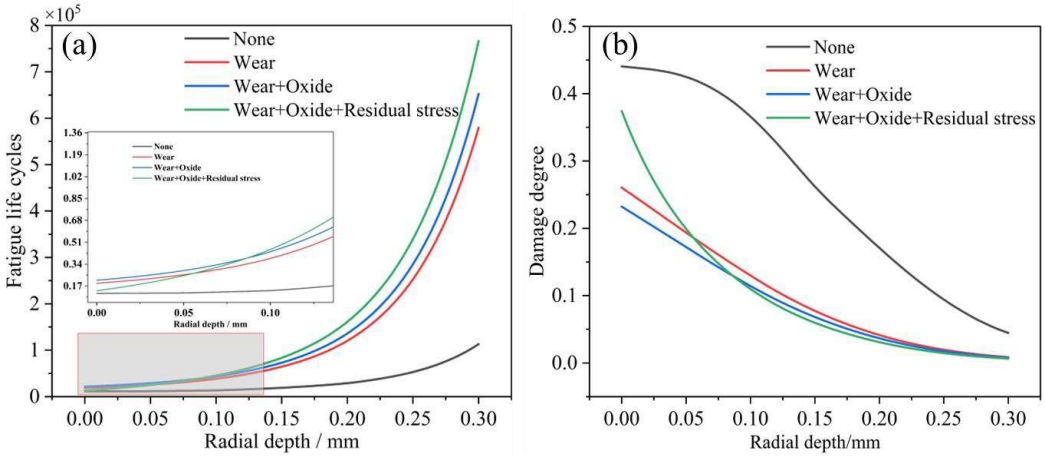


Fig. 13. Predicted fatigue life and damage distribution of the work roll: (a) fatigue life distribution under different coupling conditions, (b) damage distribution under different coupling conditions.

4.4 Damage Sensitivity Analysis

To quantify the effects of the main model parameters on fatigue damage, a local sensitivity analysis was performed around the baseline condition. Residual stress, total wear, and oxide film effect were selected as input parameters, while retained damage, maximum damage, and surface damage were used as response quantities. Each input parameter was varied independently by ±10% from its baseline value, while the other parameters were kept unchanged. The local sensitivity coefficient was defined as the normalized relative change in the response with respect to the corresponding change in the input parameter:

$$S_x = \frac{\Delta y / y_0}{\Delta x / x_0} \tag{4.22}$$

where x_0 and y_0 are the baseline input and response values, respectively. For residual stress, the initial residual stress field was scaled proportionally while preserving its radial distribution.

Fig. 14 shows the local sensitivity of mean retained damage and surface damage to residual stress, wear depth, and oxidation, with each parameter varied by ±10%. Wear depth has the largest negative sensitivity coefficients, ranging from -0.82 to -0.85. Greater material removal reduces the predicted fatigue damage by removing previously damaged material. Residual stress shows positive sensitivity, with coefficients of 0.47 for surface damage and 0.13 for mean retained damage. This indicates that surface damage is more sensitive to residual stress variations. Oxidation has a smaller negative sensitivity coefficient of approximately 0.11 for both damage measures, indicating a slight reduction in predicted fatigue damage as the oxidation-related parameter increases [35,36]. Overall, wear factor has the greatest influence on fatigue damage, followed by residual stress and oxidation. These trends are consistent within the investigated parameter range.

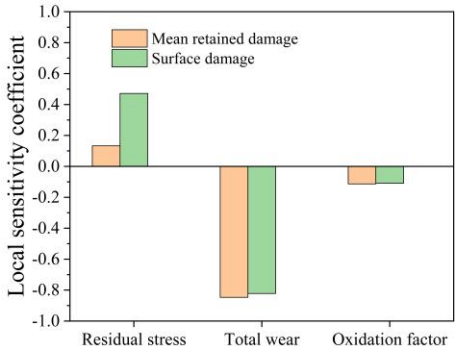


Fig. 14. Local sensitivity of fatigue damage to residual stress, wear, and oxidation

Fig. 15 shows the surface fatigue damage under different parameter combinations at 5000 rolling cycles. In Fig. 15(a), surface damage increases with the residual stress factor but decreases slightly with the oxidation factor. Fig. 15(b) shows that damage increases with residual stress and decreases with wear factor. The effect of wear is more pronounced. In Fig. 15(c), both wear and oxidation reduce surface damage, with wear showing a greater influence. Oxide films evolve during hot rolling [40]. In the present model, a thicker residual oxide film leads to greater metal-oxide interface recession under a fixed external profile change. As a result, less accumulated damage remains within the metallic substrate. These trends are consistent with the local sensitivity results in Fig. 14.

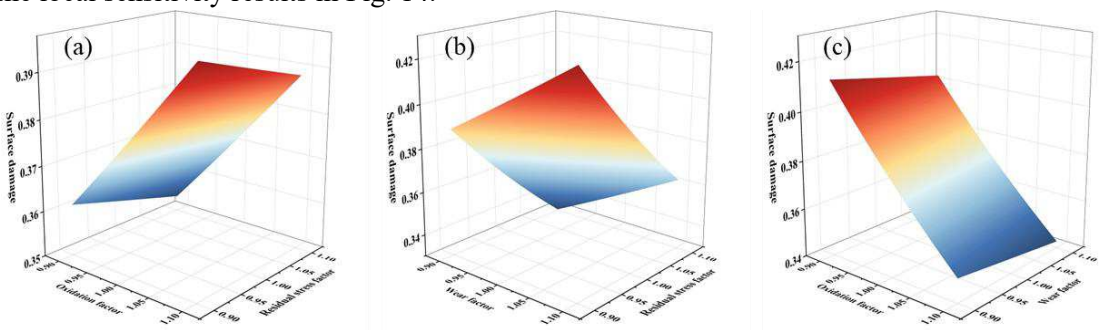


Fig. 15. Response surfaces of surface fatigue damage under different parameter combinations: (a) residual stress and oxidation, (b) residual stress and wear, (c) wear and oxidation

5. Conclusions

This study investigates the fatigue damage of hot rolling work rolls considering initial residual stress, oxidation, and wear. A coupled method is developed to account for oxide film evolution, material removal, and fatigue damage accumulation. The main conclusions are summarized as follows:

(1) Initial residual stress affects the fatigue response of the work roll. The peak equivalent strain increased from 0.0049 to 0.0077, accompanied by higher predicted surface fatigue damage. This effect weakened with increasing depth and eventually reversed, indicating that the influence of residual stress varies across the subsurface region.

(2) Oxide film evolution is governed by the competition between oxidation and wear removal. The proposed model captures the evolution of oxide film thickness, with predictions generally consistent with experimental measurements. Changes in residual oxide thickness further affect the position of the metal and oxide interface and the distribution of retained fatigue damage.

(3) The wear factor affects retained fatigue damage by controlling the amount of damaged material removed. A higher wear factor leads to lower predicted retained damage under the investigated conditions. Residual oxide thickness also influences damage retention by changing the position of the metal and oxide interface. Sensitivity analysis shows that the wear factor has the greatest effect on fatigue damage, followed by residual stress and oxidation.

It should be noted that the present model assumes uniform material removal and linear fatigue damage accumulation. Local wear variations and crack propagation are not considered. Further validation under industrial rolling conditions is therefore necessary. Nevertheless, the proposed method provides a basis for evaluating retained fatigue damage by considering the actual surface condition of work rolls. The results may provide guidance for roll degradation assessment and grinding strategies.

Acknowledgments

This work was supported by National Key R&D Program of China (2024YFE0114600); National Natural Science Foundation of China(W2633201); Youth Talent Support Program of Hebei Province (BJ2025115); Yanzhao Golden Platform Talent Recruitment Program of Hebei Province (A2025006); Innovative Capacity Cultivation Funding Project for Postgraduates of Hebei Province (CXZZBS2027022); Key Program of Scientific Research of the Department of Education of Hubei Province (D20244503).

Author Contributions

S.T.: Investigation, Writing-original draft. R.Y.: Formal analysis. J.W.: Validation. C.L.: Methodology. S.B.: Formal analysis. Y.P.: Funding acquisition. C.M.: Supervision. M.B.:

Validation. Y.W.: Validation. W.L.: Formal analysis. G.C.: Data curation. D.L.: Writing-review & editing.

Data Availability

The datasets generated and/or analyzed during the current study are available from the corresponding author upon reasonable request.

Declarations

Conflicting Interests: The authors declare no conflicting financial interests.

Reference

[1] Aigner M, Pellizzari M, Domitner J, Elizondo L, Fischbacher M, Laubichler I, et al. Influence of microstructure on degradation of cast graphitic high-speed steel. Wear 2023;522:204702. https://doi.org/10.1016/j.wear.2023.204702.

[2] Ganesh GH, Mallikarjuna Rao P, Raghushant J, Madhusudhan R. Premature failure analysis of the high-speed steel work roll of hot strip mill. J Fail Anal Prev 2024;24:2509-16. https://doi.org/10.1007/s11668-024-02034-1.

[3] Palit P, Sri KP, Kayal N, Bairwa HO, Monia S, Gokarn P, et al. Failure investigation and crack characterization of spalled work roll in hot strip mill. J Fail Anal Prev 2024;24:1522-32. https://doi.org/10.1007/s11668-024-01939-1.

[4] Wang J, Chang J, Zhang M, Li W, Peng Y. Analysis of fatigue damage of hot rolling work rolls coupled with wear effect. J Manuf Process 2024;131:1423-36. https://doi.org/10.1016/j.jmapro.2024.09.119.

[5] Salehebrahimnejad B, Doniavi A, Moradi M, Shahbaz M. Investigation of the initial residual stress effects on a work roll maximum in-service stress in hot rolling process by a semi-analytical method. J Manuf Process 2023;99:53-64. https://doi.org/10.1016/j.jmapro.2023.04.084.

[6] Meng L, Ding J, Dong Z, Sun J, Zhang D, Gou J. Prediction of roll wear and thermal expansion based on Informer network in hot rolling process and application in the control of crown and thickness. J Manuf Process 2023;103:248-60. https://doi.org/10.1016/j.jmapro.2023.08.029.

[7] Li Z, Elmi SA, Liu L, Yin B, Kuang S, Bai Z. Numerical simulation research on the temperature field and hot roll crown model of hot continuous rolling mills. Metals 2024;14:166. https://doi.org/10.3390/met14020166.

[8] Wang W, Peng W, Liu J, Li X, Sun J, Zhang D. Analysis of work roll thermal behaviour during the hot rolling process: Mathematical modelling and simulation experiments. Ironmak Steelmak 2025. https://doi.org/10.1177/03019233251324338.

[9] Sabar SK, Patel RK, Ghosh SK. Roll force prediction by combined FEM and ANN in the hot rolling process under nano-lubrication condition. Int J Adv Manuf Technol 2024. https://doi.org/10.1007/s00170-024-14326-9.

[10] Wei C, Song S, Li X, Tian Y. On-line monitoring of oxidation states in HSS work rolls

during hot rolling using pulsed eddy current testing. Int J Adv Manuf Technol 2023;126:3667-78. https://doi.org/10.1007/s00170-023-11345-w.

[11] Cheng J, Li W, Wang Y, et al. High temperature oxidation, friction and wear behavior of a high speed steel roll material. Tribology 2025;45(10):1417-1431. https://doi.org/10.16078/j.tribology.2024077.

[12] Yang Z, Zhang P, Huo X, Li G, Liu Y. Oxidation kinetics and oxide scale characteristics of Ni-containing steel at high temperature under air. Steel Res Int 2025;96:2400761. https://doi.org/10.1002/srin.202400761.

[13] Wang C, Wu H, Zhang Y. Structural transformation behavior of oxide scale during coiling of 0.9 wt% Cr-containing high-strength steel. J Mater Res Technol 2024;30:840-53. https://doi.org/10.1016/j.jmrt.2024.03.094.

[14] Konig T, Wolf E, Daum P, Kurten D, Kailer A, Dienwiebel M. Influencing factors on high temperature tribology. Wear 2025;566-567:205758. https://doi.org/10.1016/j.wear.2025.205758.

[15] Zhou M, Yan J, Wu H, Guo R, Xing Z, Jiao S, et al. Lubrication effects on the surface quality control of hot rolled steels: A review. Tribol Int 2024;199:109985. https://doi.org/10.1016/j.triboint.2024.109985.

[16] Li H, Han S, Zhang B, Qiao G, Liu J, Xiao F. Effects of niobium on microstructure, hardness and wear behavior for high-speed steel rolls. Metall Mater Trans A 2023;54:3271-85. https://doi.org/10.1007/s11661-023-07098-6.

[17] Zhang G, Liu K, Liu G, Yang B, Han P, Cao Z. Numerical study of the thermodynamic behavior and wear on the surface of hot-rolling descaling roll. JOM 2025;77:578-88. https://doi.org/10.1007/s11837-024-06933-4.

[18] Wei L, Xin Y, Xinba Y. Numerical simulation of high-temperature erosion of heat-resistant steel considering surface scale evolution. Wear 2024;550-551:205430. https://doi.org/10.1016/j.wear.2024.205430.

[19] Hu X, Zhou X, Liu H, Song H, Wang S, Zhang H. Enhanced predictive modeling of hot rolling work roll wear using TCN-LSTM-Attention. Int J Adv Manuf Technol 2024;131:1335-46. https://doi.org/10.1007/s00170-024-13105-w.

[20] Lu J, Hao L, Wang P, Huang H, Li X, Hua C, et al. Wear prediction model of hot rolling backup roll based on FEM + ML algorithm. Int J Adv Manuf Technol 2024;131:5923-39. https://doi.org/10.1007/s00170-024-13311-6.

[21] Yan X, Zhou S, Zhang H, Yi C. Degradation modeling and RUL prediction of hot rolling work rolls based on improved Wiener process. Materials 2024;17:4943. https://doi.org/10.3390/ma17204943.

[22] Peng W, Ding C, Liu Y, Sun J, Wei Z, Wang W, et al. A novel paradigm for predicting and interpreting uneven roll wear in the hot rolling steel industry. Comput Ind 2025;170:104318. https://doi.org/10.1016/j.compind.2025.104318.

[23] Opapaiboon J, Inthidech S, Ozaki K, Hashimoto M, Matsubara Y. Characteristics of fracture mechanics in cast roll materials for steel hot rolling. Int J Metalcast 2026;20:1769-84. https://doi.org/10.1007/s40962-025-01664-x.

[24] He H, Yang Q, Wang X, Xu D, Shao J, Li J, et al. Roll wear model of 4-high mill for hot strip rolling based on micro-protrusions model. Int J Adv Manuf Technol 2026;142:4889-4901. https://doi.org/10.1007/s00170-026-17402-4.

[25] Tao S, Liu C, Barella S, Li R, Guo S, Liang S, et al. Experimental study on roll wear behavior and fractal modeling under hot rolling conditions. Tribol Lett 2026;74:74. https://doi.org/10.1007/s11249-026-02166-5.

[26] Wei C, Song S, Zhang Z. Evaluation of elastic-plastic deformation in HSS work roll under coupling of residual stress thermal stress and contact stress during hot rolling. Mater Today Commun 2022;33:104613. https://doi.org/10.1016/j.mtcomm.2022.104613

[27] Kamimiyada K, Konno Y, Yanagitsuru A. Effect of heating conditions before quenching on residual stress in high-speed steel type cast iron rolls by centrifugal cast. Mater Trans 2020;61:1987-93. https://doi.org/10.2320/matertrans.F-M2020841

[28] Hu K, Zhu F, Chen J, Noda NA, Han W, Sano Y. Simulation of thermal stress and fatigue life prediction of high speed steel work roll during hot rolling considering the initial residual stress. Metals 2019;9:966. https://doi.org/10.3390/met9090966.

[29] Hu K, Shi Q, Han W, Zhu F, Chen J. On the evolution of temperature and combined stress in a work roll under cyclic thermo-mechanical loadings during hot strip rolling and idling. Materials 2020;13:5054. https://doi.org/10.3390/ma13215054.

[30] Sadeghifar M, Javidikia M, Loucif A, Jahazi M, Songmene V. Experimental and numerical analyses of residual stress redistributions in large steel dies: Influence of tempering cycles and rough milling. J Mater Res Technol 2023;24:395-406. https://doi.org/10.1016/j.jmrt.2023.03.044

[31] Aridi MR, Abdul Rafar R, Noda NA, Sun Z, Sano Y, Takata K, Takase Y. Residual stress simulation for bimetallic sleeve roll constructed by shrink-fitting in comparison with bimetallic solid roll. J Manuf Process 2023;107:252-267.https://doi.org/10.1016/j.jmapro.2023.09.068.

[32] Drobne M, Klančnik U, Fajfar P, Terčelj M. Role of oxidation and microstructure constituents on high chromium steel work roll surface degradation. J Mater Res Technol 2021;12:186-92. https://doi.org/10.1016/j.jmrt.2021.02.067

[33] Bombac D, Gintalas M, Kugler G, Terčelj M. Thermal fatigue behaviour of Fe-1.7C-11.3Cr-1.9Ni-1.2Mo roller steel in temperature range 500-700 °C. Int J Fatigue 2019;121:98-111. https://doi.org/10.1016/j.ijfatigue.2018.12.004

[34] Dreano A, Fouvry S, Guillonneau G. A combined friction energy and tribo-oxidation formulation to describe the high temperature fretting wear response of a cobalt-based alloy. Wear 2019;426-427:712-24. https://doi.org/10.1016/j.wear.2019.01.023.

[35] Yang J, Zhang W, Ta W, Yan W, Zhou Y. Prediction of oxide film growth behavior under high-temperature wear. Tribol Int 2026;224:112377. https://doi.org/10.1016/j.triboint.2026.112377.

[36] Dréano A, Fouvry S, Guillonneau G. A tribo-oxidation abrasive wear model to quantify the wear rate of a cobalt-based alloy subjected to fretting in low-to-medium temperature conditions. Tribol Int 2018;125:128-40. https://doi.org/10.1016/j.triboint.2018.04.016.

[37] Tao S, Liu R, Barella S, Liu C, Guo S, Liang S, et al. Dual driven predictive model for wear mechanism of work rolls in thin slab casting and rolling production line. Metallurgical Research & Technology 2025;122:619.

[38] Basan R, Marohnić T. A comprehensive evaluation of conventional methods for estimation of fatigue parameters of steels from their monotonic properties. Int J Fatigue 2024;183:108244. https://doi.org/10.1016/j.ijfatigue.2024.108244

[39] Raczek S, Niesłony A, Kluger K, Łukasik T. Comparison of fatigue property estimation methods with physical test data. Metals 2025;15:780. https://doi.org/10.3390/met15070780

[40] Sun W, Tieu AK, Jiang Z, Lu C, Zhu H. Theoretical and experimental investigation of thermal and oxidation behaviours of a high speed steel work roll during hot rolling. International Journal of Mechanical Sciences 2017;131-132:811-826. https://doi.org/10.1016/j.ijmecsci.2017.08.024